Low-Noise Electronic Readout for High-Throughput, Portable Biomolecular Detection in Microchannel Arrays

by

Rumi Chunara

Submitted to the Department of Electrical Engineering and Computer Science
in partial fulfillment of the requirements for the degree of

Master of Science in Electrical Engineering and Computer Science

at the

MASSACHUSETTS INSTITUTE OF TECHNOLOGY
[September 2006]
August 2006

Author .....
Department of Electrical Engineering and Computer Science
August 31, 2006

Certified by .....
Scott Manalis
Professor
pervisor

Accepted by ....
Arthur C. Smith
Chairman, Department Committee on Graduate Students

Low-Noise Electronic Readout for High-Throughput, Portable Biomolecular Detection in Microchannel Arrays

by

Rumi Chunara

Submitted to the Department of Electrical Engineering and Computer Science
on August 31, 2006, in partial fulfillment of the
requirements for the degree of
Master of Science in Electrical Engineering and Computer Science

Abstract

We have developed a new label-free detection method where specific biomolecules adsorb to the walls of a suspended microchannel resonator, or simply flow through and thereby lower its resonant frequency. The oscillation of the microchannel is measured optically by reflecting a laser beam off the channel surface and detecting its position with a photo-sensitive detector. While the optical readout is sensitive and simple to implement for single microchannels, it is less suitable for arrays since multiple laser beams and detectors must be carefully aligned for each microchannel. In contrast, the electronic readout described in this thesis is highly scalable, extremeley robust, suitable for mass production and point-of-care devices outside of the laboratory. We have investigated a variety of readout methods including capacitive amplitude sensing and strain gauges, for high signal-to-noise frequency detection that compensates for large parasitic capacitances. Implementation of capacitive detection methods result in large parasitics, indicating that piezoresistive strain gauges present the most promising solution. Integration of the piezoresistors directly on the sensors provides a one-chip solution, eliminating parasitic capacitances introduced when using multiple-chip solutions.

Once the electrical readout is optimized, for surface-based affinity assays we expect results comparable to fluorescent readout of protein microarrays.

Thesis Supervisor: Scott Manalis
Title: Associate Professor

Acknowledgments

There's not much that can be done to make research easier - but excitement and passion are two key elements of success, and two of the many things I have learned from my advisor, Scott Manalis. It has been (and will continue to be) an awesome opportunity that I am especially thankful for, to work in nanoscale sensing with him.

Perhaps the next best thing to a great advisor is having friends to work with who are equally as excited as me, more experienced, and many times smarter. I am forever indebted to all the members of the lab who have contributed to my biggest asset - knowledge. Special respek to those who bestow humour with the facts: Nebojsa, Johnson, Mike, Phil, and of course Thomas without whom I would have been in the lab a lot longer and in Europe a lot less. Thanks for coming to lab with a smile and for helping me leave with one.

Places like MIT are excellent institutions, mostly because of their students. I am thankful to all of the graduate students in other labs which are always glad to give some words of advice or spend a few hours explaining something not so trivial to me. Especially to those in Professor Rahul Sarpeshkar's laboratory, especially Soumya and Scott. I am also very lucky to have great friends outside of the lab, for constant support, empathy and for bettering my overall well-being. Also to those who have come into my life and left at some point, I have gained so many more things from you than you may realize.

Finally, to those who have probably contributed the most to my research success - without a single formula or circuit diagram, my family: Habibullah, Rosemin and Alizahra. You made me realize that as with life, struggle is the meaning of research. Defeat or victory is in the hands of God, but struggle itself is man's duty and should be his joy.

Contents

List of Figures

List of Symbols

V_{DC} - DC component of the voltage signal applied to the sense and reference capacitances

v_{AC} - AC component of the voltage signal applied to the sense and reference capacitances

C_s - dynamic portion of the SMR being sensed

C_o - overlap capacitance formed by electrode area over the substrate C_f - feedback capacitance in the first stage of the integrated circuit capacitive sensor

C_t - total capacitance at the sense node

C_p - total parasitic capacitance at the sense node of the SMR

R_p - total parasitic resistance at the sense node of the SMR

w_0 - resonant frequency in radians

w - frequency in radians

W - width of the channel in a CMOS transistor

L - length of the channel in a CMOS transistor

MTL - Microsystems Technology Laboratories, the MIT fabrication facilities

V_1 - magnitude of the voltage applied to the sense capacitance

V_2 - magnitude of the voltage applied to the reference capacitance

T_f - fixed temperature at the end of the piezoresistor closest to the base of the cantilever

T_v - variable temperature at the end of the piezoresistor closest to the tip of the cantilever

V_b - bias voltage of the wheatstone bridge used in piezoresistive detection

v_s - output voltage of the wheatstone bridge

Chapter 1

Introduction

Molecular sensing is integral to medicine and science in general. In both the clinic and laboratory, systems are constantly probed and analyzed using a variety of techniques for detection of specific analytes. As in other scientific fields, our ability to comprehend and create improves vastly once the fundamental aspects are fully understood and can be controllably manipulated. Improvements in technological capabilities unlock our ability to transduce quantitative information from biological systems, opening new portals and facilitating information from these fields. Miniaturization can play a vital role in the field and is compelling for numerous reasons including scalability, throughput, portability and robustness.

Integrated sensing tools can bring diagnostics closer to the patient in hospital, as well as provide diagnosis in areas where adequate laboratory settings and elaborate sample handling is not available. Integration of molecular tools enables early detection and timely intervention, thus optimizing use of resources on appropriate treatments. Specifically, integration enables increased sensitivity due to small sample sizes and precise control in microfluidics and microfabricated components. This will play a significant role in detection of diseases where availability of laboratory services, sensitivity and tool size play a role. In all, we believe that these tools will empower patients with greater control over their own medicinal needs wherever they are.

Integrated tools for molecular sensing can also play an important role in scientific research. Benefits arise in sensitivity, scalability and robustness when compared to

typical large-scale laboratory equipment used in molecular sensing and detection such as enzyme-linked immunosorbent assays (ELISA), surface plasmon resonance (SPR), electrophoreses gels and fluorescence microscopes. This will expand and increase our ability to detect bio-molecules in any setting. Miniaturizing molecular detection tools also promotes the ability to scale-up, increase throughput and control laboratory experiments on a level unachievable with larger equipment requirements.

In the Manalis lab, the Suspended Microchannel Resonator [3] (SMR), a novel mass detection method has been developed. The SMR is a hollow MEMS cantilever. Fluid flows through channels inside the beam. Mass changes will shift the resonant frequency, which can quantitatively convey the mass change inside. The change in mass placed at the free end of the cantilever beam in relation to a change in frequency is given as [5]:

$$\Delta m = \frac{k}{4\pi^2}\left(\frac{1}{f_1^2} - \frac{1}{f_0^2}\right) \tag{1.1}$$

where k is the spring constant of the cantilever beam, f_0 is the initial resonant frequency, and f_1 is the resonant frequency after the mass addition. Figure 1-1 below shows how the frequency response of the cantilever changes with mass.

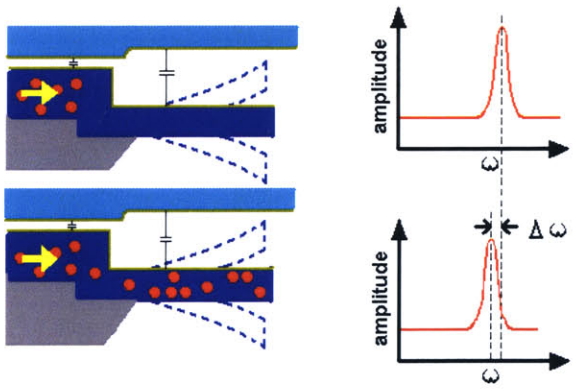

Figure 1-1: When the target molecule is present the resonant frequency shifts due to an increase in mass.

Containining the fluid inside increases mass to frequency sensitivity compared to previous techniques where the cantilever is immersed in fluid and the frequency re-

sponse is damped by the liquid. This tool can be used to sense mass increases due to density changes in the contained fluid or binding events on the interior cantilever surface. Typical molecular identification techniques involve attaching a fluorescent molecular label to the target analyte and then observing the fluorescent probe's presence optically. The SMR, in constrast, is a highly sensitive sensor which detects the presence of molecules by their mass.

The SMR can function by two unique modes. First, the sensor can be used for label-free detection where the interior of the SMR is functionalized with antibodies specific to the target analyte. If the expected antigen, for example a cancer marker, is present in the fluid, it will adsorb to the walls of the SMR, increasing the mass of the device, and thereby lower its resonant frequency. The sensor introduces a measurement technique without the undesirable consequenses of labelling. Attachment of a fluorescent label may interfere with the molecular interaction by occluding a binding site, leading to false negatives. Also precision of detection, down to the single molecule or cell level can be difficult due to limitations imposed by the optics and intensity detection algorithm. The labelling step imposes additional time and cost demands, and can in some cases interfere with the molecular interaction by occluding a binding site, leading to false negatives. On the other hand, many reporter compounds are hydrophobic, and in many screens background binding is a significant problem leading to false positives. Label-free detection avoids all of these problems.

The second method by which the SMR can function is a flow-through assay. Sample solutions can be mixed with groups of antibodies conjugated with nonparticles external to the sensor. This increases the mass of only the analyte,leading providing high sensitivity.

Typically the vibration of the SMR microchannel is measured optically using the optical lever system, common in AFM and other small-displacement measurement situations. A laser beam bounces off the channel surface and the position of the reflected spot is determined with a photo-sensitive detector as illustrated in figure 2.

While the optical readout is sensitive and simple to implement for single microchannels, it is less suitable for arrays since multiple laser beams and detectors

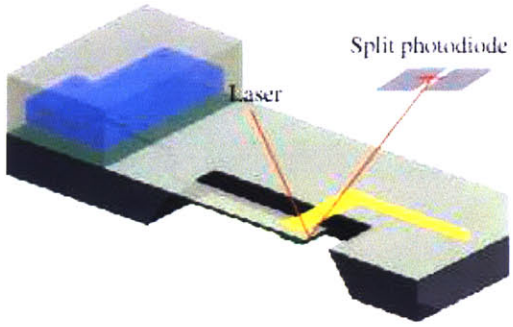

Figure 1-2: The optical lever system for measuring cantilever deflection.

must be carefully aligned for each microchannel. In contrast, electronic readout is highly scalable, suitable for mass production, and extremely robust.

As with the optical lever, support equipment for sensors are often the space-consuming components. Power and space are also limiting factors of the tools we use to convert information from our equipment to meaningful values and formats. In this thesis, we show a study of integration of electronics with the SMR sensor. Three methods of detecting the vibrations of the SMR are examined: capacitive displacement sensing using an external integrated circuit, capacitive frequency modulation using external, modular components and strain measurement using an integrated piezoresistor on the cantilever surface. Features of these designs are:

- senses very small capacitances
- opens the possibility for introducing many sensors in parallel, increasing throughput
- moves towards a more integrated, possibly portable device
- allows for in vitro studying of receptor-ligand binding for drug discovery and other scientific endeavors

In chapter 2 we discuss capacitive sensing. We show experimental results for an integrated circuit used to sense displacement of the cantilever beam. This two-chip solution measures capacitance between the cantilever surface and a suspended electrode, giving an AC output signal proportional to the displacement. We also describe how frequency modulation may be used for sensing the resonance of the

cantilever. A configuration and experimental design are outlined. Preliminary test results along with directions for further work are listed.

An integrated sensing method is discussed in chapter 3. A detailed design is described as well as an outline of how the dimensions and design are optimized for signal, noise and power.

Chapter 2

Capacitive Sensing

2.1 Capacitive Amplitude Detection

The first generation of the SMR, fabricated at MIT's fabrication laboratories, MTL, are composed of low-stress silicon nitride. Post-fabrication processing methods such as doping are complicated and also not feasible in this material. Si_3N_4 is an insulator and is not easily doped like semiconducting materials such as pure silicon. Consequently, we first looked at monitoring the motion externally, and the capacitor formed by the gold drive-electrode and chrome-coated cantilever provides an obvious candidate.

2.1.1 Capacitance: background and specifications

Capacitive detection of a cantilever resonance has previously been demonstrated in the literature [6, 14]. Similarly sensitive detection has also been demonstrated for other applications such as accelerometers and displacement detectors [1, 13]. This capacitance sensing problem is set apart from other detection problems because of the large gap between the cantilever surface and drive electrode which form the two plates of the capacitor. Figures 2-1a) and 2-1b) show two and three-dimensional renderings of the cantilever and capacitor formed by the surface and the suspended electrode.

Capacitance between two surfaces varies inversely with the distance between them.

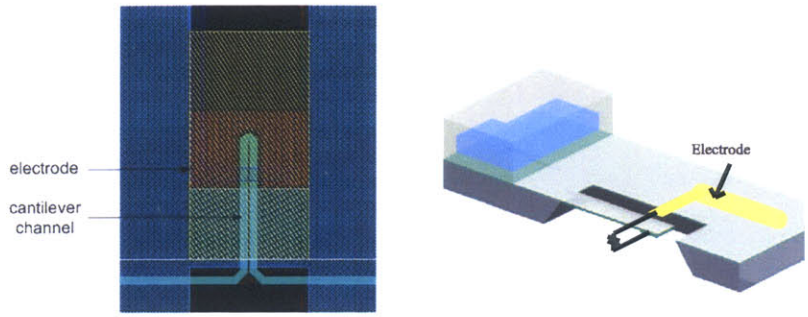

(a) (b)

Figure 2-1: 2D and 3D rendering of the cantilever and suspended electrode.

Although it follows that the capacitive signal increases linearly with a smaller gap size between the two plates (in this case the electrode on the upper pyrex surface and the cantilever surface), squeeze-film damping due to the close proximity of the pyrex surface to the cantilever, as shown in figure 2-2 decreases the quality factor [10]. This force increases as the inverse gap distance cubed [3], so the final dimensions were chosen to balance these effects: readout, electrostatic actuation as well as capabilities of the fabrication process.

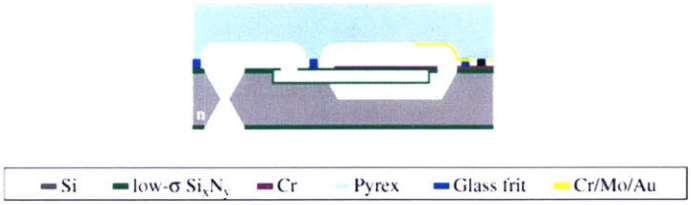

Figure 2-2: Cross section of the SMR, showing the electrode under the pyrex surface.

The capacitance of the device can be modeled as a static capacitance, formed by the overlap area of the electrode over the cantilever and substrate of the MEMS chip in parallel with the dynamic capacitance between the electrode and tip of the cantilever which changes at approximately 40kHz at resonance. The gap between the pyrex and cantilever is 70 μm in the cavity area, and the overlap gap between the pyrex and substrate is 20 μm. This results in a total capacitance of 100fF. The capacitance is modulated when the cantilever vibrates. To estimate the change in capacitance, we

assume the change in gap between the electrode and cantilever is sinusoidal over time, and use the maximum change in distance. For a maximum beam deflection of of 1 μm [2], the change in capacitance is only 0.01fF. An electrical model of the system is shown in figure 2-3.

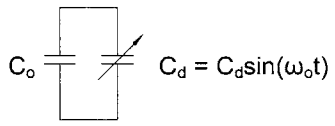

Figure 2-3: An electrical representation of the static overlap capacitance (C_o) in parallel with the harmonic capacitance (C_d) formed between the tip of the cantilever and electrode.

The bandwidth for the measurement is constrained by how quickly measurements are to be made. For example, our bandwidth of detection is determined by how quickly we expect molecular-binding events to occur. We estimate that we will have at least 1 second to observe each change, giving a bandwidth of 1Hz.

2.1.2 Readout technique

The natural frequency of micromechanical resonators may be measured through observation of the amplitude and phase response to an external driving source, as outlined in [3]. For more sensitivity and larger dynamic range, the drive frequency should be tuned close to the resonant frequency of the device, which is best accomplished by a closed-loop system (see figure 2-4). Closing the loop on the system allows the drive frequency to be brought close to the natural resonant frequency of the device, giving an improved vibration amplitude and better frequency response/quality factor. Ideally an electronic readout system would include a sensing component, an appropriate phase and amplitude adjustment, and feedback to drive the cantilever. First, we focus on the sensing aspect and the following discussion relates to an open-loop, drive-and-sense design.

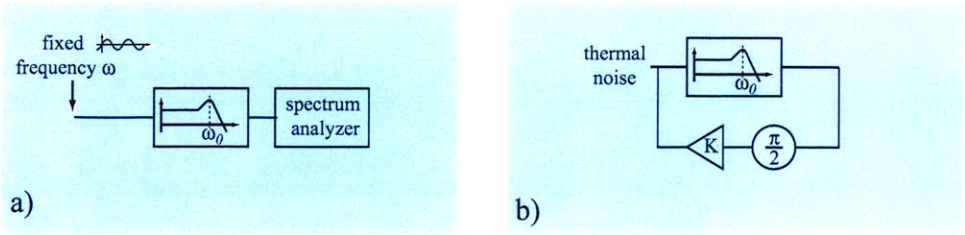

Figure 2-4: Block diagrams of sensing schemes: a) open loop drive and sense, b) closed loop.

2.1.3 Electronics and MEMS integrated system description

One of the ways capacitive sensors have been successfully implemented with MEMS resonators is through processing the CMOS and MEMS components on the same wafer [6, 14]. Fabrication of the MEMS structures on a pre-processed CMOS wafer decreases parasitic capacitances immensely. However, due to the great complexity and complications involved in such a process we choose to attack the problem as a two-chip solution. The MEMS and sensor chips are fabricated separately; the MEMS chip at MTL, and the CMOS at the MOSIS foundry in California. The chips are connected via a wirebond. This introduces large parasitic capacitances. The wirebond itself is mostly inductive, but parasitics from the wire to ground degrade the signal to be sensed. To decrease these effects, the two chips were placed in the same cavity of a package to decrease the distance between the connected nodes. The final package is pictured in figure 2-5.

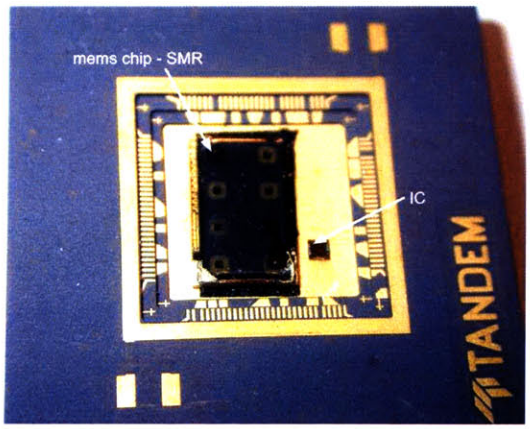

Figure 2-5: Package containing the MEMS and IC chips.

The circuit designed is a two-stage amplifier with a maximum gain of 56 dB and 1MHz 3dB bandwidth. The large bandwidth allows the possibility of using the amplifier as a direct sensor, with an output at the resonant frequency of the SMR, or as an amplifier of an amplitude-modulated signal with a carrier frequency up to 1MHz.

The drive signal used to actuate the cantilever has a DC and AC component. The DC component, V_{DC}, is large (60V) to increase cantilever deflection. This is ultimately limited by the pull-in voltage. The AC component, v_{AC} is chosen large enough to excite the cantilever harmonically: 1V for this device. Figure 2-6 shows an electrical model of the system with the drive and sense signals of the SMR and how they connect to the amplifier.

At resonance C_s, the capacitance being sensed is harmonic (modelled as $C_s \sin(\omega_o t)$) and the current induced includes a component from the static capacitance and AC voltage (feedthrough) as well as the DC voltage and dynamic capacitance.

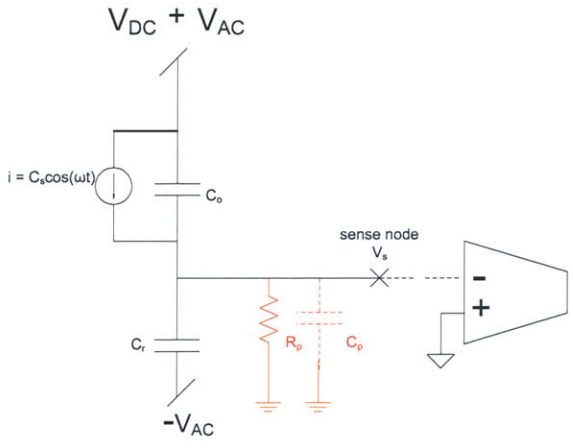

Figure 2-6: Scheme of how the current induced by movement of the cantilever results in a voltage signal which is amplified.

$$
\begin{aligned}
I &= \frac{\delta Q}{\delta t} \\
&= \frac{\delta}{\delta t}(VC) \\
&= V_{DC}\frac{\delta C_s}{\delta t} + v_{AC}C_o \\
&\approx 0.39 V_{DC} C_s \omega_o \cos\omega_o t + v_{AC}C_o
\end{aligned} \tag{2.1}
$$

In equation 2.1 current resulting from the total voltage (V) over the total capacitance (C) is calculated. The resulting voltage on the sense node can be estimated from the signal current over the parasitic impedance, Z_p, as illustrated in figure 2-6.

$$
\begin{aligned}
v_s = i \quad Z_p \\
Z_p \quad = R_p \parallel Z_{Cp}
\end{aligned} \tag{2.2}
$$

As equation 2.1 makes clear, the signal component is $V_{DC}\frac{\delta C_s}{\delta t}$, and the feedthrough component is $v_{AC}C_o$. The factor 0.39 is a correction factor that accounts for a normalized average deflection [7]. The parasitic capacitances at the sense node can originate from external and on-chip sources; any area between the sense node and ground. Major sources are the connection between the MEMS and IC (estimated at approximately 500fF), and on the IC the dominant sources are C_{gs}, C_{gb}, (25fF and 10fF respectively from simulation). Thus the total C_p is approximately 535fF. There is also a DC impedance at the sense node which is realized through a diode-connected pmos transistor [4]. The effecitvc resistance between drain and source is on the order of Gigaohms, so these two in parallel provide the total parasitic impedance. Given $V_{DC} = 60V$, $\omega = 2\pi 40kHz$ and $C_s = 0.01fF$, the voltage signal induced at v_s is approximately 0.1 mV.

2.1.4 Circuit details

Because the signal to be sensed is extremely small it is important that the input referred noise from the integrated circuit is low enough for an acceptable signal-to-noise ratio. Input capacitance should also be minimized. As illustrated above, any parasitic capacitance at the sense node to the substrate/ground node will decrease the signal at the sense node decreases as $1/C_p$ with parasitic capacitances.

Input noise was minimized by using a single source-follower stage input. Figure 2.7 shows the measured and simulated input-referred noise spectral density of the whole amplifier.

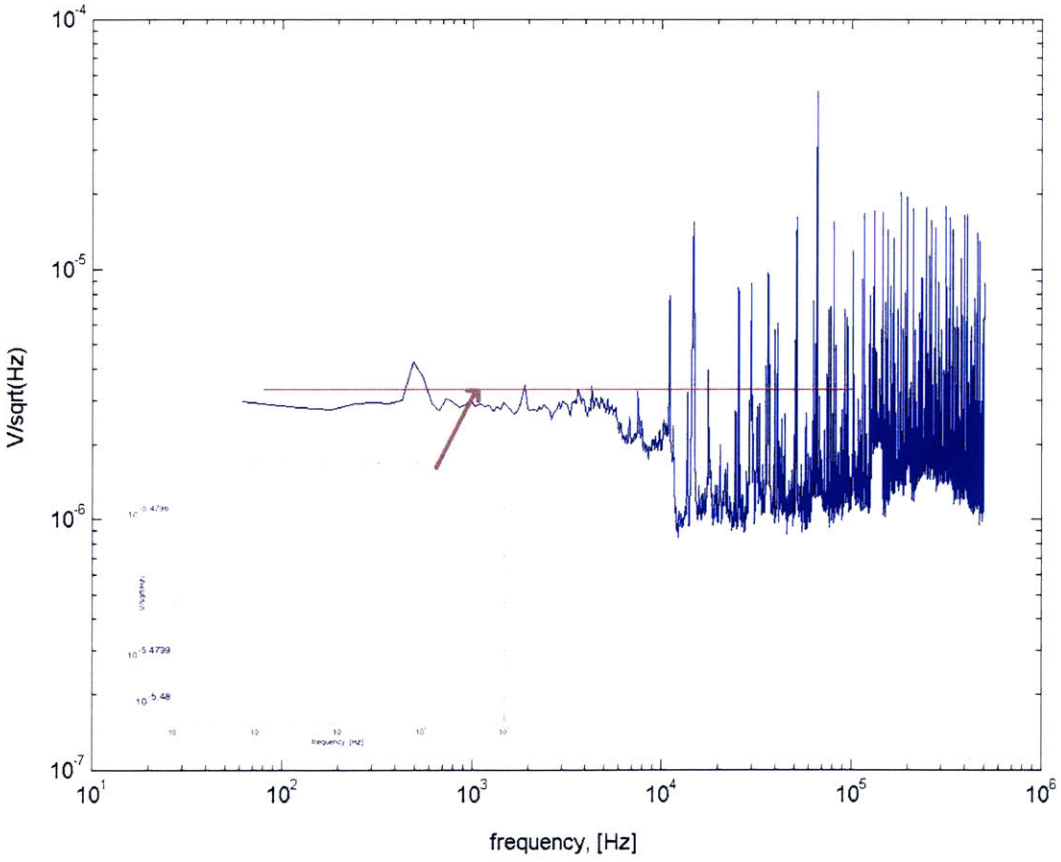

Figure 2-7: Experimentally measured noise and simulated noise superimposed. An expanded version of the simulated spectrum is inset.

The measured and simulated spectra are of the same order of magnitude, however the

bias values for the chip determined through experimentation are different than those determined by simulation, as explained below. Also the high variability present in the experimental measurement (10^4 Hz and above) is attributed to external noise sources that could not be eliminated. Because the input referred noise, i_n, from a single NMOS transistor scales with the ratio of the width to length, W/L: $i_n^2 = 4kTg_m df$, it is desired to minimize the W/L ratio. While keeping noise to a minimum, it is also desirable to amplify the actual signal. The gain of the common-source stage is $g_m R_o$, where g_m is the gain of the stage. Above threshold $g_m = \kappa \mu C_{ox} \frac{W}{L}$. So it turns out that the W/L ratio is an important factor in increasing gain but decreasing the noise. Typically, the DC value of a source-follower is set using a feedback resistor between the input and output nodes (gate and drain). In this application, since minimizing all parasitics at the sense node is desired, a resistor here would increase the input capacitance through the miller effect (show figure). The second stage of amplification is a simple 5-transistor operational transconductance amplifier, OTA.

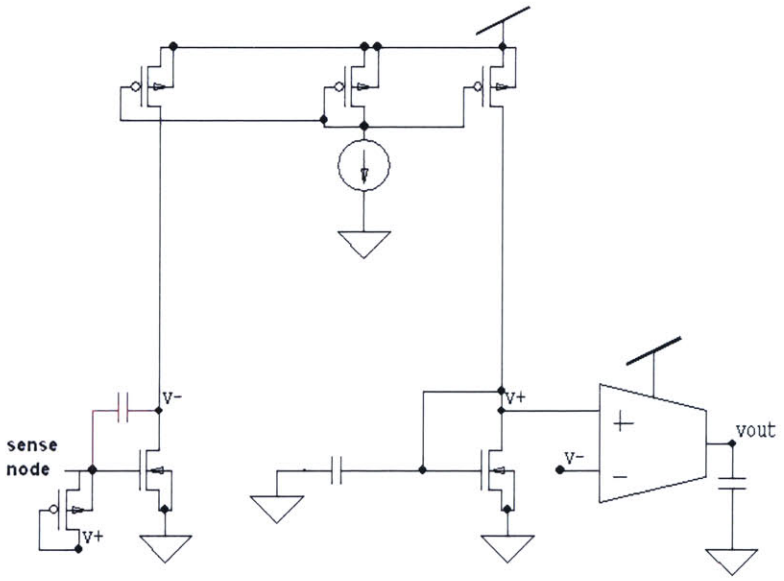

Figure 2-8: Scheme of the fabricated integrated circuit (red feedback capacitor included in some versions of the chip).

A dual-input amplifier is important for the second stage to set the DC point of

the sense node. Because the sense node from the MEMS chip is electrically floating, the DC value at the input of the amplifier would otherwise also be floating. The node could drift and saturate the amplifier. To get around this effect, the DC point of this node is fixed using a dummy source follower of identical dimensions, but with the input node (AC) grounded. This serves to balance the inputs of the second stage amplifier (dual-input) as well as decrease parasitics at the sense node. Because the AC capacitance being sensed is so small, the AC feedback on the first amplification stage is also delicate. The gain of the first stage can be modelled as a simple inverting amplifier (as in figure 2-9), and is given by:

$$\frac{V_{out}}{V_s} = \frac{C_f}{C_t} \tag{2.3}$$

where C_f is the feedback capacitance and C_t is the total capacitance to ground at the sense node. In this case, $C_t = C_o + C_{ref}$. This output signal however, is degraded in the presence of parasitics at the sense node, which results in:

$$\frac{V_{out}}{V_s} = -\frac{G}{1 + G\frac{C_f}{C_t}} \tag{2.4}$$

where G is the gain of the amplifier. Considering system values, the output voltage of the first stage is degraded with C_p by approximately half.

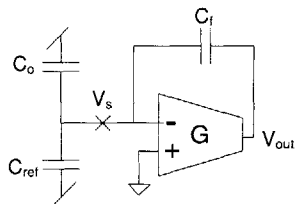

Figure 2-9: Diagram of the first stage of amplification, which can be modelled as a simple inverting amplifier with AC feedback.

From equation 2.3 it is clear that to increase the gain of the stage, it is wise to decrease the size of C_f below C_{in}. However, since C_{in} is only a fraction of a femto-farad, it is difficult to design a capacitive feedback of less than this size around the

common-source first stage. A few versions of the same circuit with slight differences were fabricated in an attempt to create a small, stable and calibrated feedback capacitance. In one case, no explicit capacitor was implemented, with the hope that stray capacitances between the metal lines for the input and output of the input stage would be enough to close the loop. In a second case, a definite overlap capacitance of 10fF was implemented.

2.1.5 Capacitance: results and obstacles

In implementation of the method proposed we faced many associated challenges. As mentioned earlier, it was important to design a very small feedback capacitance in the first stage of amplification to decrease the initial loss in signal as much as possible. However, the capacitance implemented (both when relying on parasitics or the designed 10fF capacitance) is so small that essentially the result is an open-loop amplifier which is very difficult to bias stabily. The current biases on the two input common source stages have to be carefully tuned to the microamp level. Without the right biases, the amplifier will saturate to the power or ground level because of the high open-loop gain.

Also due of the high gain, any unwanted signal is amplified through the amplifier. This interferes greatly with sensing the actual signal which is extremely small, and can be smaller than unwanted signals. One major source of unwanted signal is feedthrough from the static capacitance portion of the device (equation 2.1) . A reference capacitor was used in order to cancel the feedthrough signals. As illustrated in figure 2-6, the current from the static portion of the capacitance should amount to the exact opposite of that from the reference capacitor due to the negative AC voltage applied on the reference capacitor. Since there is no DC bias on the reference capacitor, there should be no mechanical response of the reference cantilever. However, mismatches in fabrication lead to femtofarad differences in the size of the reference and device cantilevers. In order to completely cancel the two signals, phase and amplitude of the AC voltage signals applied at each electrode can be carefully tuned. Matching phase and amplitude exactly however, is a difficult problem in itself. Figure 2.6 shows how

we may represent the contributions from C_o and C_r. In each case there is a voltage contribution at the sense node through a voltage divider between C_o or C_r and the parasitics. Equation 2.1 gives the exact magnitude of the voltage signal at the sense node, leaving the amplitude and phase of the input and reference signals variable. The contributions from C_o (V_{Co}) and C_r (V_{Cr}) are:

$$\mid V_{Co} \mid = \frac{\sqrt{(V_1 \omega C_o R_p)^2 + (\omega^2 V_1 C_o R_p (C_o R_p + C_r R_p + C_p R_p))^2}}{1 + \omega^2 (C_o R_p + C_r R_p + C_p R_p)^2} \tag{2.5}$$

$$\mid V_{Cr} \mid = \frac{\sqrt{(V_2 \omega C_r R_p)^2 + (\omega^2 V_2 C_r R_p (C_r R_p + C_o R_p + C_p R_p))^2}}{1 + \omega^2 (C_r R_p + C_o R_p + C_p R_p)^2} \tag{2.6}$$

Figure 2-10 shows how well the two must be matched compared to the size of the expected signal. If V_1, V_2, ψ_1 and ψ_2 vary exactly to cancel any difference between C_o and C_r, then the resulting signal at the sense node would be 0.

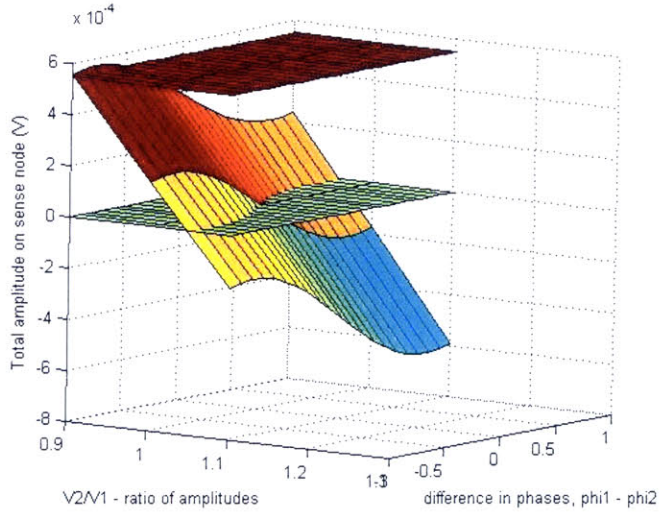

Figure 2-10: A plot of the feedthrough amplitude (multicolored plane) varying applied AC voltage amplitude and phase. The red (top) plane shows the magnitude of the signal, and the green (bottom) plane shows perfectly cancelling the reference and overlap signals.

The anticipated difference between C_o and C_r, attributed to fabrication imperfections, is approximately 10-15 fF, or 10-15%.

To get around this matching problem, using a new generation of the SMR fabri-

cated with two electrodes under one cantilever was considered. This way, one electrode could be used to actuate, and the signal could be read from the second electrode. Although this would avoid the matching problem because there would be no feedthrough signal from the static capacitance (no AC applied at the sense electrode), coupling between the two electrodes causes the same problem.

Capacitive amplitude sensing proves to be very difficult to implement for the current versions of the SMR. Compared to other capacitive readout integrations with resonant MEMS cantilevers, the large separation between the cantilever surface and counter electrode in this case decreases the capacitance to be sensed and consequentely the induced voltage level. Amplification of this very small signal without amplifying signals from the same source is a challenge. Further difficulties result because of parasitic capacitances which are unavoidable in a two-chip solution. In the following chapters we explore other methods of electronic readout for the SMR.

2.2 Sensing through frequency modulation

Previously we attempted to measure the change in the capacitance formed by the cantilever and the drive electrode through amplitude detection. This method proves difficult mostly due to feedthrough and parasitics which result in a low signal-to-noise ratio. The dominant noise is white noise, which is flat across the frequency spectrum. The amplitude of the noise varies randomly at all frequencies. In our system, the noise could be picked up in the displacement sensing system and appear at the output which is difficult to distinguish from the actual signal. FM systems are inherently immune to random noise. In order for the noise to interfere it would have to modulate the AC signal at the correct frequency. In a second implementation, we make use of this inherent benefit of frequency modulation.

2.2.1 FM Implementation

Implementation of the frequency modulation technique is based on a previous demonstration also with a resonant cantilever [12]. It became possible to try this method

of electronic sensing once a generation of SMRs with two electrodes under each cantilever were fabricated. One electrode located under the base is used to drive the cantilever, and the capacitive signal is sensed from the other, under the tip. The resonant frequency of these devices is close to 200kHz. As illustrated in figure 2-11, one electrode is used as a connection to the VCO and the drive signal is connected to the other electrode. The sense electrode overlaps the cantilever in an area approximately $100\mu m$ by $90\mu m$, resulting in a capacitance change very similar to the previous version of the SMR, approximately 0.01fF. The same electrode cannot be used for both purposes as in the amplitude detection case because of the bias that is necessary on the drive electrode. The input to the VCO cannot be at such a large DC potential.

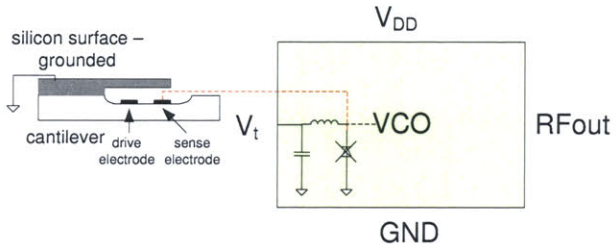

Figure 2-11: Connection details of the two electrodes to the VCO. Tuning node shunt capacitor and AC block inductor are bypassed.

The resonant cantilever is used to modulate the frequency of the external VCO. The VCO is a Clapp oscillator with a varactor diode as the frequency determining element. As the DC bias across the varactor changes, the effective capacitance between the anode and cathode varies, moving the oscillation point of the VCO.

A modular component manufactured by Crystek (figure 2-12) was chosen for this application. We chose a modular component, as it was important to ensure that the SMR chip could easily be connected to the VCO. Being modular also allows easy alteration of the package and contents without a long time-lag for fabrication. Another important selection criteria was a high enough frequency.

For frequency modulation, the carrier frequency is chosen usually at least ten times higher than the modulation frequency. Also, as the frequency increases, the internal

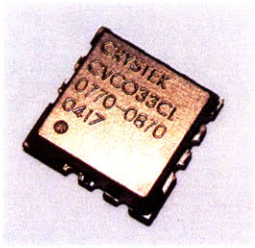

Figure 2-12: Photo of the VCO used. Manufactured by Crystek Corporation, it is a contained, modular package.

capacitance and inductance component values decrease. In this implementation the cantilever replaces the varactor element, and a static capacitance is placed in parallel with the cantilever to ensure the oscillation still occurs. This static capacitance becomes smaller the higher the oscillation frequency of the VCO. As will be shown, the smaller this capacitance, the easier it is to realize the modulating signal.

The varactor diode is removed and connected to the cantilever as shown in figure 2-11. The cantilever could not be connected externally to the tuning node, because there is an inductor which acts as an AC block at that node, and the cantilever AC frequency would not modulate the VCO frequency. The cantilever is connected to the VCO through a wirebond.

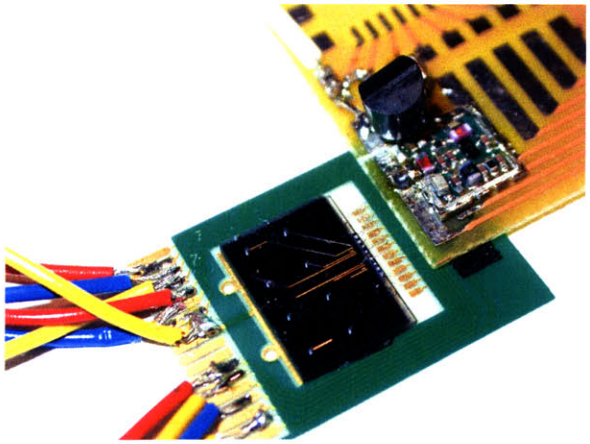

Figure 2-13: Photo of the FM technique implementation. The MEMS chip (left) and VCO (right) are connected via a wirebond.

2.2.2 Specifications and detection scheme

Essentially, the static capacitance in parallel with the cantilever is a parasitic capacitance. Parasitics also impact sensitivity in this scheme but through a different manner than in the amplitude sensing method.

To understand this effect, first it is important to understand how frequency modulation works. The modulation index, β, is defined as:

$$\beta \equiv \frac{\Delta f}{f_m} \tag{2.7}$$

the ratio of the frequency deviation Δf to the modulation frequency, f_m. We can estimate Δf for our system by the tuning sensitivity for the VCO (in Hz/V), the change in capacitance per change in potential for the original frequency determining element, and the capacitance change expected from the cantilever.

$$\Delta f = \frac{\Delta f}{\Delta V} \times \frac{\Delta V}{\Delta C} \times \Delta C \tag{2.8}$$

The modulation index comes into play when we consider the spectrum of the signal that results from the frequency modulation process. The time domain signal is given by [9]:

$$s(t) = \cos(2\pi f_c t + \beta \sin(2\pi f_m t)) \tag{2.9}$$

Assuming the carrier frequency, f_c, is large enough compared to the bandwidth of the FM signal, we can rewrite this as:

$$s(t) = Re[\tilde{s}(t) \exp(j2\pi f_c t)] \tag{2.10}$$

where $\tilde{s}$(t) is the complex envelope of the FM signal s(t), defined by and expanded in the form of a complex Fourier series by:

$$\tilde{s}(t) = A_c \exp[j\beta \sin(j2\pi f_m t)] = \sum_{n=-\infty}^{\infty} c_n \exp(j2\pi f_m t) \tag{2.11}$$

where c_n, the coefficients of the fourier expansion, are equal to $A_c J_n(\beta)$, where $J_n(\beta)$ is recognized as the nth order Bessel function of the first kind with argument β. Substituting back into the equation for the FM signal, and interchanging the order of summation and evaluation of the real part, gives:

$$s(t) = A_c \sum_{n=-\infty}^{\infty} J_n(\beta) \cos[2\pi(f_c + nf_m)t] \tag{2.12}$$

Fourier transformation shows that

$$S(f) = \frac{A_c}{2} \sum_{n=-\infty}^{\infty} J_n(\beta)[\delta(f - f_c - nf_m) + \delta(f + f_c + nf_m)] \tag{2.13}$$

Thus it is clear that the resulting signal will have peaks at the carrier component, $\pm f_c$, as well as an infinite series of side frequencies located at $\pm f_c \pm nf_m$ where the amplitude of the peaks will depend on $J_n(\beta)$, n=0 being the carrier peak. In our case, since β is small compared with unity, only the Bessel coefficients $J_0(\beta)$ and $J_1(\beta)$ have significant values, so the frequency spectrum is effectively composed of a carrier and a single pair of side frequencies at $f_c \pm f_m$, as in figure 2-14. Evaluating $J_1(\beta)$ for our values gives an amplitude of -80dBm. Parasitic capacitances will decrease the modulation index because the change in capacitance will effectively be lower, the more static capacitances are between the sense node and ground. This will lower the amplitude of the side peaks.

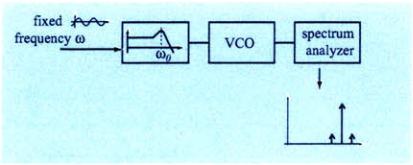

Figure 2-14: Block-representation of the open-loop frequency modulation technique.

It is desirable in this method also to run the system in the a closed loop, which will shift the drive frequency close to the natural frequency of the resonator, increasing the maximum amplitude and thus the maximum capacitance shift. In a closed loop system, the output of the VCO (the modulated signal), would have to be mixed down

to a lower frequency. One possibility is to mix directly down to baseband, but as in radio receivers, the signal is often mixed down to a lower frequency at which filtering can be done, but still avoids noise at DC which can cause DC shifts. For initial testing, however, the resonant frequency was determined prior to implementation and the device was driven at resonance. A DC and AC component were applied at the drive electrode and the sense electrode was connected to the VCO. The output of the VCO was monitored with a spectrum analyzer as illustrated in figure 2-14.

2.2.3 Troubleshooting and future investigation areas

A major problem encountered after implementing the setup in this method was coupling of the drive signal to the output. The drive signal also modulates the VCO frequency, and appears at $f_c \pm f_m$ in the frequency domain. It would be impossible to distinguish this signal from the actual cantilever signal since they both appear at the same frequency and have the same phase. Because the drive signal is multiplying in, we deduce that the signal must be present at a node which connects to a nonlinear/multiplication unit in VCO, most likely the amplification module. Likely possibilities are the power or ground busses because they cover large areas providing many places for signals to couple-in. A voltage regulator was applied between power and ground of the VCO in an attempt to keep the power node more stable. Also bypass capacitors were connected between power and ground to ground any noise signals. A possible means by which the drive signal is coupling into the power or ground lines is capacitive coupling through the air. A test to confirm this suspicion, by bringing alligator leads on a BNC cable connected to a function generator close to the VCO, resulted in the same effect. The amplitude of this coupled signal is approximately -80dBm below the carrier amplitude. This is the approximate expected magnitude of the signal (see above calculation), and thus will interfere with the readout. To reduce coupling through the air, various techniques to shield signals and reduce antenna effects were implemented. Alligator leads act as antennas, so were twisted, shielded and finally were replaced with a plain BNC connection directly from a function generator to the cantilever. This technique reduced the coupled signal but

not by more than a few dBm, requiring other ways of reducing the signal.

Impedance mismatches in connections between the chips, as well as connections to power and ground could cause reflections that would radiate signals into the air. Therefore it should be ensured that all lines are 50Ω impedance. Another technique which could reduce or eliminate the problem is to actuate the cantilever mechanically, thereby removing a drive signal from the immediate vicinity of the MEMS chip and VCO.

Chapter 3

Piezoresistive sensing

As alluded to earlier in this thesis, fabrication of a new generation of SMRs in silicon opens up new electronic readout possibilities. In particular, piezoresistance can be implemented by doping the silicon substrate. Piezoresistance is an established property first discovered over 200 years ago. The first exploitation of the property in a silicon sensor was demonstrated in 1969 [8]. In the biological realm, a silicon surface is easier to functionalize than silicon nitride, Si_3N_4. Thus, the new material allows us to implement sensing methods with ease as well as electronic methods that have been tried and tested in the past.

3.1 Piezoresistance property

Piezoresistivity is the effect whereby the bulk resistivity of a material depends on the mechanical stress applied to it. Physically, the resistance changes when the material is stressed due to deformation of energy bands. This allows electrons to move between or within the valence and conduction bands with more or less ease, changing the conductance. The effect is dependant on the stress components parallel and perpendicular to the direction of the current flow, $\sigma_{\parallel}$ and $\sigma_{\perp}$. The fractional change in resistivity, ρ, is quantified through the linear combination:

$$\frac{\Delta\rho}{\rho} = \pi_{\parallel}\sigma_{\parallel} + \pi_{\perp}\sigma_{\perp} \tag{3.1}$$

where the constants $\pi_{\|}$ and $\pi_{\perp}$ are the *piezoresistive coefficients* in the parallel and perpendicular directions (to the direction of current). The coefficient values depend on many factors including crystal orientation, doping type and concentration.

The piezoresistive coefficient for silicon is highest in p-doped base. However, our devices are made of p-doped silicon so we are limited to using n-dopants for the resistor. In $\{110\}$ wafers, the piezorsistive coefficient is maximal in the $\langle 100 \rangle$ direction ($\pi_{\|} = -102$, negative implying a decrease in resistance with stress). However this would require that the resistors are oriented 45° to the wafer flat, adding a great deal of complexity to the fabrication process. Thus the resistors fabricated are n-type in the $\langle 110 \rangle$ direction in which $\pi_{\|} = -32$.

3.2 Design of piezoresistor sensors

There is a large base of knowledge and experience in creating and using piezoresistors, clearing up a lot of uncertainties in the design phase. As suggested in [15], the piezoresistor design should confine the resistor to the portion of the cantilever nearest the base. This is because maximum stress occurs at the base of the cantilever, while there is zero stress at the tip. Extending the resistor over the full length of the cantilever decreases the stress, averaging 50% of the maximum stress. If the resistor only occupies the half of the cantilever nearest the base, the average stress is 75% of the maximum. To take advantage of this effect we confine the resistor to the quarter of the cantilever closest to the base. The relative size and structure can be observed in figure 3-1. The size is also optimized for other parameters as outlined in section 3.3. The basic structure of the resistor is simple: the resistive n doped region and n+ doped traces used to connect the resistor to metal bondpads (not shown). High conductance traces are used because the top pyrex layer cannot be bonded on top of metal.

In order to measure small changes in the resistance, R_{cant}, we use a common technique for measuring unknown resistances which is ubiquitous in piezoresistance measurments; the wheatstone bridge. Through this method the change in resistance is

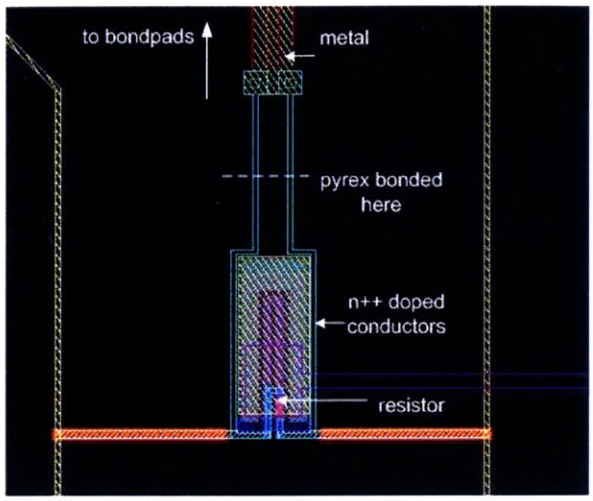

Figure 3-1: 2D CAD drawing of the cantilever, showing the resistor and highly doped contact traces.

converted to a voltage signal, which is amplified in a differential amplifier to eliminate other sources of voltage change. The inputs of the amplifier are biased to matching DC values using known resistances. A schematic of the readout electronics is pictured in figure 3-2. Because the exact value of the cantilever resistance is unknown, a tunable resistor is used in the position R_4 to ensure zero DC potential difference at the inputs of the amplifier.

The doping level for the resistor was determined through literature studies. As illustrated in figure 3-4, the piezoresistance factor, which is multiplied by the piezoresistance constant to allow for variation due to temperature and doping level, increases as doping level decreases. In our application, because the cantilevers are hollow it is important that the junction depth of the implant-substrate is not too big. If so, the implant layer would connect to the inside of the cantilever and make an electrical connection to the fluid inside (see the cross-section in figure 3-3).
The junction depth, x_d, is the distance at which the concentration of p-type dopants equals the concentration of n-type dopants and is given as:

$$x_d = \sqrt{\frac{2\epsilon_{si}}{q}\left(\frac{1}{N_a}+\frac{1}{N_d}\right)(\phi_t - V_a)} \tag{3.2}$$

where ϕ_t is the built-in potential, equal to $V_t \ln \frac{N_a N_d}{n_i^2}$. V_t is the threshold voltage,

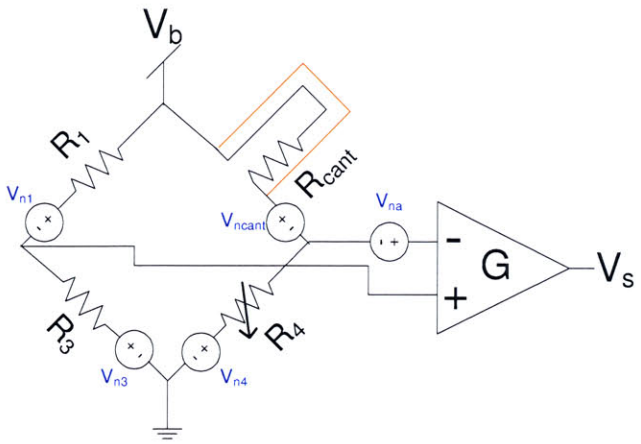

Figure 3-2: Complete circuit used to measure the deflection of the cantilever including representations of all noise sources.

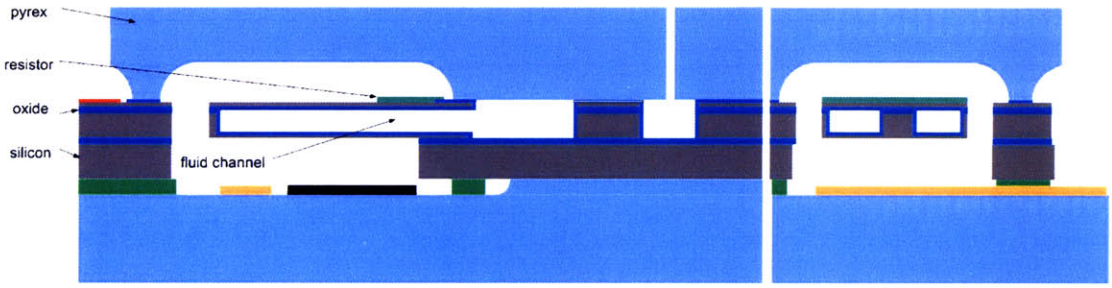

Figure 3-3: Cross section of the silicon devices on which piezoresistors are implanted.

N_a and N_d are the acceptor and donor dopant concentrations respectively, n_i is the intrinsic carrier concentration of silicon, V_a is the applied bias voltage (0V in our case), and ϵ_{si} is the dielectric permittivity of silicon. Through the equation we see that it decreases by the square root, but increases as the natural logarithm of the built-in potential. As suggested in [15], a dopant concentration of $2 \times 10^{18} cm^{-3}$ gives an appropriately large piezoresistive factor. This results in a junction depth of $1.01 \times 10^{-6} m$. An order of magnitude drop in the n-dopant concentration, from 2×10^{18} to 2×10^{17} only decreases the depth by $0.06 \mu m$. Doping level for the conductive traces is $1 \times 10^{20} cm^{-3}$ which makes the silicon essentially as conductive as a metal.

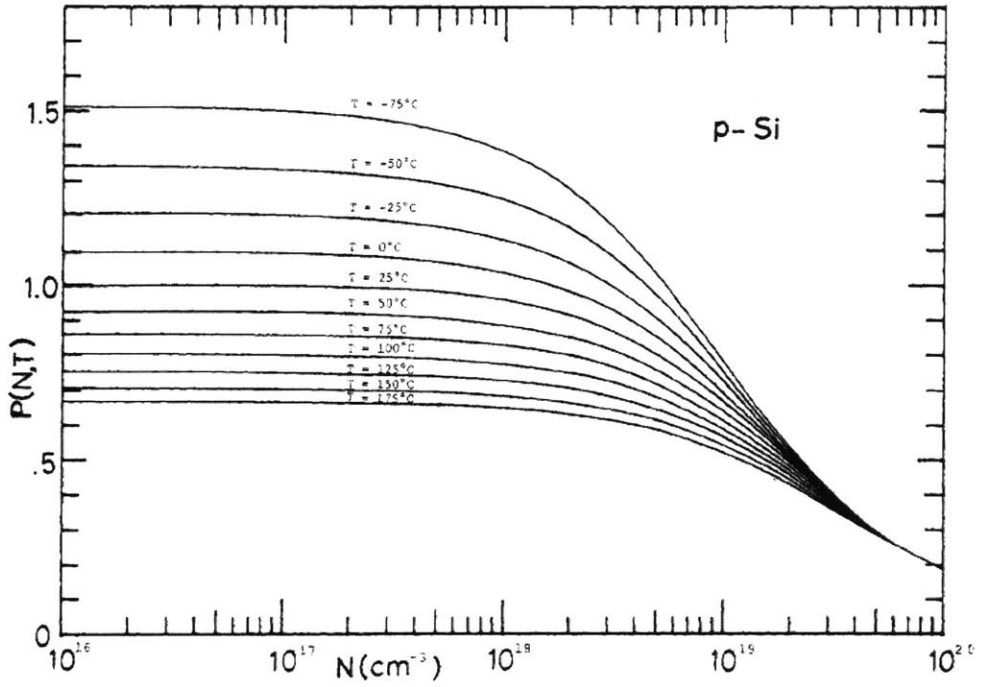

Figure 3-4: Piezoresistance factor P(N,T) as a function of impurity concentration and temperature for p-Si [11].

Because the piezoresistive coefficients are particular to direction and crystal structure, the gauge factor, K, which relates fractional change in resistance to strain is often used. K relates to $\pi_{\|}$ by Young's modulus, Y.

$$K = Y \times \pi_{\|} \tag{3.3}$$

The gauge factor in pure silicon is approximately 100 [15]. We can estimate the strain (the change in length per unit length, $\Delta L/L$) of the cantilever geometrically. Electrostatically we estimate the cantilever will deflect by approximately 100nm. Figure 3-5 shows this length increase in part a), as well as the geometry used to extrapolate the change in length given 100nm maximum deflection.

First, figure 3-5a), shows the right-angled triangle formed by the length of the cantilever and the mid-point deflection distance, z, to find the hypoteneuse, h.

$$h = \sqrt{L^2 + z^2}$$

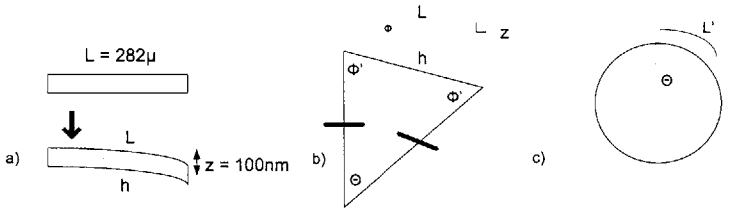

Figure 3-5: Geometry used to estimate the strain of the cantilever when deflected: a) and b) show calculation of the angle the strained cantilever surface subtends, and c) shows calculation of the new length.

This length is the same as the non-equal length side in the isosceles triangle in figure 3-5b). Using the known angle ϕ', θ and then ϕ can be calculated:

$$\begin{aligned} \tan\phi &= \frac{z}{L} \\ \phi &= \arctan\frac{z}{L} \\ \phi' &= 90 - \phi \\ \Theta &= 180 - 2\phi', \end{aligned} \tag{3.4}$$

$$\begin{aligned} \frac{h}{\sin\Theta} &= \frac{h'}{\sin\phi'} \\ h' &= \frac{h\sin\phi'}{\sin\Theta} \end{aligned} \tag{3.5}$$

The length of the arc the angle ϕ subtends, L', is calculated by equating the ratio of 360° to the circumference of the circle with radius $h' + t/2$, with the length of the arc L' to the angle ϕ :

$$\frac{L'}{\phi} = \frac{2\pi(h' + t/2)}{360^\circ} \tag{3.6}$$

$$L' = 2.800056679 \times 10^{-4} m \tag{3.7}$$

For this device then, we can estimate the normalized change in resistance as:

$$\begin{aligned} \frac{\Delta R}{R} &= K\frac{\Delta L}{L} \\ &= K \times \frac{L' - L}{L} \\ &\approx 2 \times 10^{-3} \end{aligned} \tag{3.8}$$

3.3 Design parameters

The base resistance and consequently size of the resistor was determined to optimize the signal to noise ratio of the resistor. In addition, we would like to minimize the power dissipated in the resistor to decrease temperature increases which can alter biological substrates inside the cantilever.

3.3.1 Power constraints on design

The power dissipated over a resistor is given as:

$$P = \frac{V^2}{R}$$

and in our case is:

$$P = \frac{V_b^2}{R_{cant}} \tag{3.9}$$

where V_b is the bias across the piezoresistor on the cantilever, R_{cant}. Clearly, power increases linearly with a decrease in the base resistance of the piezoresistor and to minimize power we would increase the the resistance. Once R_{cant} is selected, we pick V_b to ensure the power dissipated is less than $100\mu W$. This is explained further in section 4.4.1.

3.3.2 Noise

Figure 3-2 shows the complete circuit: cantilever and external electronics including noise sources. The dominant noise is white noise; at our resonant frequency of 100kHz we are above the $1/f$ noise corner. As evaluated previously [15], the output-referred rms noise of the circuit in figure 3-2 is:

$$v_n = G\sqrt{\frac{1}{4}[(v_{n1}^2 + v_{n2}^2 + v_{n3}^2 + v_{n4}^2 + v_{amp}^2]} \tag{3.10}$$

The input-referred noise of a resistor, v_{nx} is $\sqrt{4k_BTR\Delta f}$ where k_B is the Boltzmann constant, T the temperature and Δf the bandwidth of measurement. The input-referred noise of the external amplifier will be as low as $4nV/\sqrt{Hz}$. If we make R_{cant} large enough, the amplifier noise will be negligible compared to the noise from all of the resistors and we can neglect v_{amp} leaving the noise mostly under our design control. The noise can also be minimized by choosing R_1 and R_3 values small. As described above, R_4 has to match R_{cant}.

The size of our piezoresistor, R_{cant}, is thus constrained by the power (desire R_{cant} large enough so that the power dissipation is low) and the noise (make R_{cant} small so the noise isn't too large). This places the size on the order of a few $k\Omega$. We select a design value of $1k\Omega$ and for a target power dissipation of $100\mu W$, the voltage bias should be:

$$\begin{aligned} P = & \ \frac{V_b^2}{R_{cant}} \\ V_b & = \sqrt{100\mu W \times 1k\Omega} \approx 300mV \end{aligned} \tag{3.11}$$

The magnitude of the resistance in ohms is equal to:

$$R = \frac{\rho L}{A} \tag{3.12}$$

Physical dimensions of the piezoresistor are constrained in part by the geometry of

the SMR. The length, L, of the piezoresistor is restricted to the bottom-quarter of the cantilever for reasons described above. The width of the resistor is constrained by the fact that it must fit within the width of the cantilever. We have less control over the cross-sectional depth of the resistor. The implants will diffuse in based on the concentration and energy of the implants, as well as further processes such as oxidation and annealing that heat the dopants. We aim to keep the implants shallow, as the top lid of the cantilever is only $3\mu m$ deep (see figure 3-3). To obtain the desired concentration of dopants as described above in section 4.2 but not diffuse too deeply, we use a high implant dose and low energy. The exact values were selected through simulation of the implant depth using the program SUPREME and the following figure shows a cross-section with dopant levels.

3.3.3 Voltage signal from piezoresistors

Once the magnitude of R_{cant} is determined, we can confirm that we will have a large enough signal-to-noise ratio. The voltage output signal from the amplifier, v_s, can be derived from the output of the wheatstone bridge and our estimate of the fractional change in resistance, giving:

$$v_s = \frac{V_b R_4}{R_4 + R_{cant} + \Delta R} - \frac{V_b R_1}{R_1 + R_2} \tag{3.13}$$

If $R_4 = R_{cant}$ and $R_1 = R_2$, this becomes:

$$v_s = \frac{G V_b \Delta R}{2(2R + \Delta R)}$$

and for ΔR small compared to R, bias voltage, V_b of 300mV and a gain of 500 from the operational amplifier,

$$\begin{aligned} v_s &= \frac{G V_b \Delta R}{4R} \\ &\approx 75mV \end{aligned} \tag{3.14}$$

note that R_4 must be tunable in order to account for uncertainty in the exact value

of R_{cant}. Because the theoretical noise and signal values can be estimated it is best to check if our expected fractional change in resistance, $\frac{\Delta R}{R}$, is above the minimum fraction by a reasonable amount. The minimum detectable normalized resistance change is found by examinging a signal-to-noise ratio of one. Equating v_s and v_n:

$$\frac{\Delta R}{R}min = \frac{4\sqrt{2k_BTR\Delta f}}{V_b} \tag{3.15}$$

with a design value of $1k\Omega$ for R_{cant}, and bias voltage, V_b of 300mV this gives a minimum detectable fractional resistance of 3.8×10^{-8} which is below the expected change by a factor of 10^5.

3.3.4 Temperature effects from piezoresistors

Since the electrical resistance of the doped material depends upon collisonal processes within the substrate, resistance increases with temperature due to increased number of electron collisions. For biological experiments, temperature stability is extremely important inorder to prevent alteration of the substrate, for example denature of proteins. Accurate temperature measurements will require us to understand the temperature dependancies of the device. The piezoresistive coefficients vary with temperature, as shown in figure 3-4, however this is not the dominant effect. The temperature of the cantilever will increase primarily due to power dissipation through the resistor. Thermal conductivity of a material is defined as the quantity of heat, Q, transmitted in time t through a thickness L, in a direction normal to a surface of area A, due to a temperature difference ΔT, under steady state conditions, when the heat transfer is dependent only on the temperature gradient.

$$j = \Delta Tk \tag{3.16}$$

where

$$k = \frac{Q}{t} \times \frac{L}{A\Delta T} \tag{3.17}$$

Let us consider the cantilever as a pure silicon beam with one end fixed in temper-

ature (the end connected to the bulk silicon, and thus the end of the resistor closest to this side is also fixed in temperature). Due to power dissipation, the temperature at the other end of the resistor changes depending on the bias voltage. The temperature from this end of the resistor across the rest of the cantilever must be the same, as the cantilever is suspended in air, and there is no medium through which the heat can dissipate. The temperature change is calculated from the thermal conductivity:

$$P = (T_f - T_v)k \tag{3.18}$$

where T_f and T_v are the fixed and variable temperatures respectively, in kelvin, $P = Q/t$ is the power dissipated as calculated in section 4.3.1, and k is the thermal conductivity of silicon, $148\frac{W}{mK}$, which we multiply by the cross sectional area of the resistor and divide by the distance between T_f and T_v, length of the resistor in our case. This gives a T_v of 270K.

3.4 Results and future work

Fabrication of the newest SMRs in silicon with the implanted piezoresistors is underway. The process includes integration of the SMR with a nano-concentrator device. Therefore the process has many steps and is extremely time-intensive. An early step in the process involves fusion bonding two SOI wafers in order to create completely insulated inner channels (see fig 3-3). This step is still being refined, and in the group of wafers that have been bonded and through the implantation process, failures were observed in the bonding near the cantilever lid, resulting in degredation of the cantilevers, and rendering the devices unusable. The low yield has been a setback, but processing of the remaining steps is continuing in the hope to obtain some preliminary results and shape the design for future lots.

Test wafers were also implanted at the same time as the actual device wafers. These wafers were patterened with the same mask as the device wafers, and have resistor and contact implants of the exact same geometry. However, there are no cantilevers etched nor silicon wafers fusion bonded. The base resistance, R_{cant}, was

measured at $3.956k\Omega$. This is within an order of magnitude of the designed value, the difference most likely resulting from shallower implants than simulated. Pending completed devices, the external amplifier and electronics will be optimized for noise to increase AC sensitivity of the piezoresistor.

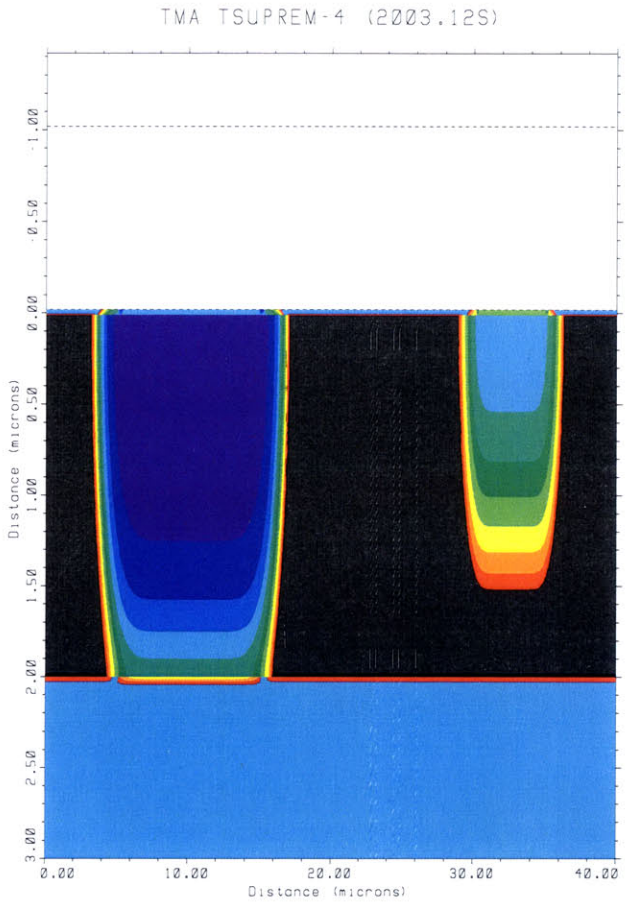

Figure 3-6: Cross-section of silicon showing concentration of dopants after simulating all processing steps; x = 5-15 shows the n++ doped region and x = 30-35 the resistive n region. Traversing downwards through the silicon, the conductive region dopant concentration starts at 10^{20} at the surface, in the purple region. The resistive region varies from 10^{18} in the cyan region (closest to the surface where distance = 0) to $10^{13} cm^{-3}$ in the red region (further into the silicon).

Chapter 4

Conclusions and Future Work

Sensing any kind of signal involves transduction from one medium to another. Scientific capabilities have evolved to a point where we are able to convert information from the biological realm into other forms of data we are more used to dealing with. This will expand our knowledge of processes and signals in this area - allowing applications in areas previously unthinkable.

The work outlined in this thesis provides insight on ways biological signals can be transduced to electronic signals. This decreases the size and number of components needed for the sensor. Besides the physical benefits of integration, converting the signal to an electronic value also provides ease of transferability to other systems as well as an easy to interpret output format.

In general, the techniques examined deal with issues of:

- transduction of signals from biological system to electronics
- integration of electronics with and readout from MEMS
- low-noise techniques for measurement
- designing around extremely small capacitances
- frequency detection

It was found that the main problems encountered in building this type of system include feedthrough from drive signals and parasitic capacitances. For these reasons, the method considered in chapter 3, piezoresistance, is the most promising.

Once fabrication of all of the electronics is complete and optimized, particular applications that exploit the scalability and integration provided through electronic readout will be studied. Focus will move from the output of the sensor to the interface between the biosensor and the chemical or biological system to be studied. Combining these studies with design of arrays of the SMR sensor, enabled by electronic readout will create a highly sensitive, high-throughput and portable sensor.

Appendix A

Supreme Code

```
$ dec. 18 - simulating conductor and metal implant laterally
$ setup grid
$ start with p wafer/oxide layers
$ grow thermal oxide (before implantation)
$ implants

$ setup grid
LINE X LOC=0 SPAC=.2 tag=left
LINE X LOC=40 SPAC=.2 tag=right
LINE Y LOC=0 SPAC=.05 tag=topsi1
LINE Y LOC=2 SPAC=.05 tag=topox1
LINE Y LOC=3 SPAC=.05 tag=topsi2


$ start with <100> p-type wafer
region oxide1 ylo=topox1 yhi=topsi2 xlo=left xhi=right


$ calculate this conc. based on resisitivity
INIT <100> IMPURITY=boron I.RESIST=20

$ oxidize before implanting
$ thin oxide - want 20-30nm
DIFFUSION TEMP=950 TIME=60 DRYO2
EXTRACT OXIDE X=0 THICKNES


$ n++ implant (for conducting contact)
DEPOSITION PHOTORES THICKNES=1.5
```

```
ETCH PHOTORES START X=5 Y=0
ETCH CONTINUE X=15 Y=0

ETCH CONTINUE X=15 Y=-2
ETCH DONE X=5 Y=-2
IMPLANT PHOSPHORUS DOSE=4e15 ENERGY=150 TILT=7
ETCH PHOTORES ALL

$ n+ implant
DEPOSITION PHOTORES THICKNES=1.5
ETCH PHOTORES START X=30 Y=0
ETCH CONTINUE X=35 Y=0
ETCH CONTINUE X=35 Y=-2
ETCH DONE X=30 Y=-2
IMPLANT PHOSPHORUS DOSE=1.5e14 ENERGY=150 TILT=7
ETCH PHOTORES ALL


$ deposit nitride layer
DEPOSITION NITRIDE THICKNES=1

$ thin pad oxide $ target ~ 50nm
$DIFFUSION TEMP=1000 TIME=60 DRYO2
$EXTRACT OXIDE X=2.5 THICKNES
$EXTRACT OXIDE X=15 THICKNES
$EXTRACT OXIDE X=22.5 THICKNES

$ dopant anneal
DIFFUSION TEMP=1050 TIME=240 INERT

OPTION device=ps-c file.sav=n+.ps
SELECT Z=LOG10(PHOSPHORUS)
PLOT.1D X.VALUE=32.5 LINE.TYP=1 COLOR=2
$SELECT Z=LOG10(DOPING)
$PLOT.1D X.VALUE=32.5 ^AXES ^CLEAR LINE.TYP=1 COLOR=5
SELECT Z=PHOSPHORUS
PRINT.1D X.VALUE=32.5 OUT.FILE=phos32.5.dat
SELECT Z=DOPING
PRINT.1D X.VALUE=32.5 OUT.FILE=doping32.5.dat

$OPTION device=ps-c file.sav=n.ps
$SELECT Z=LOG10(PHOSPHORUS)
$PLOT.1D X.VALUE=7.5 ^AXES ^CLEAR LINE.TYP=1 COLOR=2
$SELECT Z=LOG10(DOPING)
$PLOT.1D X.VALUE=7.5 ^AXES ^CLEAR LINE.TYP=1 COLOR=5
```

```
OPTION device=ps-c file.sav=n++.ps
SELECT Z=LOG10(PHOSPHORUS)
PLOT.1D X.VALUE=10.0 LINE.TYP=1 COLOR=4
$SELECT Z=LOG10(PHOSPHORUS)
$PLOT.1D X.VALUE=10.0 ^AXES ^CLEAR LINE.TYP=1 COLOR=2
$SELECT Z=LOG10(DOPING)
$PLOT.1D X.VALUE=10.0 ^AXES ^CLEAR LINE.TYP=1 COLOR=5

$SELECT Z=BORON
$PRINT.1D X.VALUE=12.5 OUT.FILE=boron12.5.dat
SELECT Z=PHOSPHORUS
PRINT.1D X.VALUE=32.5 OUT.FILE=phos32.5.dat
SELECT Z=DOPING
PRINT.1D X.VALUE=32.5 OUT.FILE=doping32.5.dat

OPTION device=ps-c file.sav=p.ps
SELECT Z=LOG10(BORON)
PLOT.1D X.VALUE=2.5 LINE.TYP=1 COLOR=4
$SELECT Z=LOG10(PHOSPHORUS)
$PLOT.1D X.VALUE=2.5 ^AXES ^CLEAR LINE.TYP=1 COLOR=2
SELECT Z=LOG10(DOPING)
PLOT.1D X.VALUE=2.5 ^AXES ^CLEAR LINE.TYP=1 COLOR=5

SELECT Z=BORON
PRINT.1D X.VALUE=2.5 OUT.FILE=boron2.5.dat
SELECT Z=PHOSPHORUS
PRINT.1D X.VALUE=2.5 OUT.FILE=phos2.5.dat
SELECT Z=DOPING
PRINT.1D X.VALUE=2.5 OUT.FILE=doping2.5.dat

OPTION device=ps-c file.sav=lateral.ps
SELECT Z=LOG10(DOPING)
PLOT.2D X.MIN=0 X.MAX=40 Y.MAX=3 LINE.TYP=2
COLOR MATERIAL=SILICON COLOR=1
COLOR MATERIAL=OXIDE COLOR=5
FOREACH X (15 TO 20 STEP .5)
COLOR MIN.VALUE=X MAX.VALUE=(X + .5) COLOR=((2 * (X - 15)) + 8)
```

Bibliography

[1] B. Amini, S. Pourkamali, and F. Ayazi. A high resolution, stictionless, CMOS compatible SOI accelerometer with a low noise, low power, $0.25\mu m$ CMOS interface. *IEEE Journal of Solid-State Circuits*, 39, 2004.

[2] T.P. Burg. *Suspended microchannel resonators for biological detection.* PhD thesis, Massachusetts Institute of Technology, 2005.

[3] T.P. Burg and S.R. Manalis. Suspended microchannel resonators for biomolecular detection. *Applied Physics Letters*, 83:2698, 2003.

[4] M. Tavakoli Dastjerdi. Analog VLSI circuits for inertial sensory systems. Master's thesis, Massachusetts Institute of Technology, 2001.

[5] Chen G.Y.. et al. Absorption-induced surface stress and its effect on resonance frequency of microcantilevers. *J. Appl. Phys.*, 77, 1995.

[6] Forsen E. et al. Ultrasensitive mass sensor fully integrated with complementary metal-oxide-semiconductor circuitry. *Applied Physics Letters*, 87, 2005.

[7] Verd J. et al. High-sensitivity capacitive readout system for resonant submicrometer-scale cantilever based sensors. *IEEE International Symposium on Circuits and Systems*, 5, 2005.

[8] C.M. Gieles. Subminiature silicon pressure sensor transducer. *Digest IEEE International Solid-State Circuits Conference*, 1969.

[9] Simon Haykin. *Communication Systems, 4rd Edition*, chapter 1.2. Wiley, 2000.

[10] H. Hosaka, K. Itao, and S. Kuroda. Damping characteristics of beam-shaped micro-oscillators. *Sensors and Actuators, A: Physical*, 49, 1995.

[11] Y. Kanda. A graphical representation of the piezoresistance coefficients in silicon. *IEEE Trans. Electr. Dev.*, 64, 1982.

[12] S.J. Kim, T. Ono, and M. Esashi. Capacitive resonant mass sensor with frequency demodulation detection based on resonant circuit. *Applied Physics Letters*, 88, 2006.

[13] Z. Liu, Q.A. Huang, and W. Li. A differential capacitive mini-displacement sensor. *Proceedings of IEEE Sensors*, 3, 2004.

[14] G. Shekhawat, S.H. Tark, and V. Dravid. Mosfet-embedded microcantilevers for measuring deflection in biomolecular sensors. *Science*, 311, 2006.

[15] M. Tortonese. *Force sensors for scanning probe microscopy.* PhD thesis, Stanford University, 1993.